Investigation of NO reduction by CO reaction over oxidized and reduced NiOx/CeO2 catalysts

Journal:	*Catalysis Science & Technology*
Manuscript ID	CY-ART-07-2021-001215.R1
Article Type:	Paper
Date Submitted by the Author:	23-Sep-2021
Complete List of Authors:	Lee, Kyung Min; Stony Brook University, Materials Science and Chemical Engineering Kwon, Gihan; Brookhaven National Laboratory, Photon Science Division - National Synchrotron Light Source II Hwang, Sooyeon; Brookhaven National Laboratory, Center for Functional Nanomaterials Boscoboinik, Jorge; Brookhaven National Laboratory, Center for Functional Nanomaterials Kim, Tae Jin; Stony Brook University, Materials Science and Chemical Engineering

SCHOLARONE™
Manuscripts

Investigation of NO reduction by CO reaction over oxidized and reduced NiO$_x$/CeO$_2$ catalysts

Kyung-Min Lee [1], Gihan Kwon [2], Sooyeon Hwang [3], Jorge Anibal Boscoboinik [3], Taejin Kim[1]*

[1] Materials Science and Chemical Engineering Department, Stony Brook University, Stony Brook, NY, 11794, U.S.A

[2] National Synchrotron Light Source II, Brookhaven National Laboratory, Upton, NY 11973, U.S.A

[3] Center for Functional Nanomaterial, Brookhaven National Laboratory, Upton, NY 11973, U.S.A

Corresponding Author: * TJK: Materials Science and Chemical Engineering Department, Stony Brook University, Stony Brook, NY 11794, taejin.kim@stonybrook.edu

ABSTRACT

CeO_2 supported NiO_x catalysts have been widely studied in various catalytic reactions including NO reduction by CO. This work is mainly focused on investigation of the impact of catalyst synthesis conditions (e.g., oxidation and reduction) on the physicochemical properties of NiO_x/CeO_2 catalyst and the catalytic response for NO reduction by CO reaction. The oxide NiO_x/CeO_2 sample was prepared by the incipient wetness impregnation (IWI) method and reduced under hydrogen reduction treatment at high temperatures (500 and 700 ^{o}C). Physiochemical properties of the synthesized samples were characterized by BET, Raman spectroscopy, XRD, XPS, EELS and high-resolution transmission electron microscopy (HR-TEM). The results showed that higher reduction temperature led to the decrease in specific surface area (SSA), less oxygen vacancy/defect site, larger crystallite size of CeO_2 support, and formation of metallic Ni on the surface. The oxidized NiO_x/CeO_2 catalyst showed the highest catalytic activity, indicating that the presence of oxygen vacancy/defect site, Ni^{2+} oxidation state, and smaller crystallite size are believed to enhance the catalytic activity. The *in-situ* DRIFTS study confirmed the generation of several intermediate species, such as nitrate, carbonate, and N_2O. On the basis of *in-situ* DRIFTS and activity results, the possible reaction mechanism of NO reduction by CO over NiO_x/CeO_2 was proposed.

Keywords: NO reduction, Carbon monoxide, Nickel oxide, Cerium oxide, Physicochemical properties

Introduction

With the rapid development of automotive industry and technology, toxic gas pollutants (CO, NO_x, hydrocarbons (HC), particulate matters (PMs), volatile organic compounds (VOCs), etc.) have been accumulated during the past few decades, which are harmful to humans (i.e., CO poisoning) and threaten the earth's ecosystem (i.e., ozone layer depletion and climate change). Among the environmental pollutants, nitrogen oxide (NO_x) is considered as one of the primary atmospheric molecular contaminants, which is emitted from vehicle exhaust, power plants, and the fuel combustion.[1-4] The NO reduction by CO reaction ($2NO + 2CO \rightarrow N_2 + 2CO_2$) has gathered more attention due to the simultaneous elimination of two pollutants.[5,6]

Supported platinum group metals (PGMs) catalysts, such as Pt, Pd, Ru and Rh, have been extensively investigated due to their high catalytic performance for NO reduction by CO reaction.[7-11] However, considerable effort has been exerted to reduce the usage of PGMs catalysts due to the PGMs' high cost, scarcity, and high processing temperatures.[12-14] Therefore, it has been paid more attention to supported transition metal oxides (e.g., CuO_x, FeO_x, CoO_x, and NiO_x) as alternative materials.[15-20] Among the transition metal oxides, nickel oxide is a promising catalyst showing both high catalytic activity and stability in several chemical reactions, such as CO oxidation, steam reforming of ethanol, and dry reforming of methane as well as NO reduction by CO reaction.[21-25] With strong correlation among the oxidation state of Ni, the property of support materials and the catalytic activity have been extensively investigated to achieve improved catalytic properties of NiO_x. K. Tang et al., studied the effect of the CeO_2 supported various Ni species on the catalytic activity for NO reduction by CO, and concluded that both NiO on surface and Ni^{2+} in the Ni-Ce-O solid solution are active sites.[22]

The authors also reported that CeO_2 (110) facets provides more active sites to Ni species compared to the CeO_2 (100) facets. Y. Wang et al., reported the support effect on the NO reduction by CO over the NiO/MO_x (M=Al, Ti, and Ce) catalysts, and concluded that CeO_2 supported NiO showed higher catalytic activity than that of Al_2O_3 and TiO_2.[21] The authors claimed that oxygen vacancies on CeO_2 support and reduced CeO_2 surface are crucial for high activity and N_2 generation, while Ni oxidation state was not clear. D. Lopes et al., proposed that reduced form of copper and nickel on the Cu-Ni bimetallic catalyst could be active site during the NO reduction by CO.[26] The authors compared the He and H_2 pretreated Cu-Ni bimetallic catalyst and observed a significant increase of catalytic activity with H_2 pretreatment condition. Although several literatures reported a structure-catalytic performance relationship over CeO_2 supported NiO_x or $Ni-Ce-O_x$ solid solution catalysts, a pretreatment effect (i.e. reducing temperature) on catalyst structure and catalytic activity was not fully studied.

The focus of this study is to investigate the impact of catalyst synthesis conditions on the physicochemical properties of NiO_x/CeO_2 catalysts and on the catalytic response for the NO reduction by CO reaction. The oxidized NiO_x/CeO_2 sample was reduced under hydrogen reduction treatment at high temperatures. The oxidized and reduced catalysts were analyzed by BET, ICP-MS, Raman, XRD, XPS, EELS and HR-TEM measurement to characterize the physicochemical properties of the catalysts. The GC and DRIFT techniques were applied to exam the catalytic activity and selectivity in addition to the intermediate species detection.

Experimental Section

Catalyst Synthesis

The supported nickel oxide (NiO_x) catalysts were synthesized using incipient wetness impregnation (IWI) method. First, the desired amounts (10wt%) of nickel (II) nitrate hexahydrate (98%, $(Ni(NO_3)_2 \cdot 6H_2O$, Alfa Aesar) were completely dissolved in de-ionized water to make precursor solutions. Then the precursor solution was added to ceria powder (HAS 5, Rhodia) drop by drop while mixing constantly. After adding all the precursor solution, the mixture was dried at room temperature overnight and further dried at 120 °C for 12 hours in air (Airgas, Dry air, 20% oxygen and 80% nitrogen) in a combustion boat with a tube furnace (Lindberg/Blue Mini-Mite, Thermo). Finally, the catalyst was treated in air at 400 °C for 6 hours to complete the calcination process and sieved (425 μm, Fieldmaser). The synthesized ceria supported nickel oxide catalysts were denoted as 10% NiO_x/CeO_2. In the case of reduced catalysts, the 10% NiO_x/CeO_2 catalysts were first treated under N_2 atmosphere at 400 °C for 30 min and then reduced in H_2 flow (5 vol % H_2 balanced with N_2, flow rate of 50 mL min^{-1}) at 500 °C and 700 °C for 3 hours. The reduced catalysts were denoted as 10% NiO_x/CeO_2-500R and 10% NiO_x/CeO_2-700R, respectively. The as-received bulk CeO_2 samples were treated in the same ways (calcined at 400 °C, reduced at 500 °C, and reduced at 700 °C) as described above and denoted as CeO_2-Oxi, CeO_2-500R and CeO_2-700R.

Characterization

Nitrogen adsorption and desorption isotherms (N_2-isotherms) were performed using a Micromeritics ASAP 1010. The specific surface area (SSA) and pore volume of catalysts were calculated using the multipoint Brunauer-Emmett-Teller (BET) and Barrett-Joyner-Halenda (BJH) methods, respectively. Prior to N_2-isotherm measurement, the catalysts were degassed at 300 °C for 4 hours under vacuum to remove impurities and volatiles. The Ni contents of the NiO_x/CeO_2 (oxidized and reduced) catalysts were determined by the ICP-AES (Agilent 7500cx quadrupole inductively-coupled plasma mass spectrometer) method. The samples were

5

dissolved in 2% nitric acid and the actual concentrations of Ni contents were calculated based on nickel standard calibration curves. Morphology and chemical distribution of NiO_x/CeO_2 catalysts were analyzed by transmission electron microscopy (TEM). The high-resolution TEM images, scanning TEM-energy dispersive X-ray spectroscopy (STEM-EDX) elemental maps, and electron energy loss spectroscopy (EELS) were obtained with a Thermo-Fisher Talos F200X at an accelerating voltage of 200 kV. The EELS spectra of supported NiO_x were acquired using a Gatan Enfinium spectrometer. The Raman spectra of bulk CeO_2, bulk NiO, and supported NiO_x catalysts were obtained with visible (532 nm, Horiba Raman spectrometer) laser (laser power = 100 mW). The visible Raman spectra were collected in the $200\sim1400$ cm^{-1} Raman shift regions. For each scan, the acquisition time was 10 seconds and the final spectrum was accumulated from 60 scans. To obtain high energy X-ray diffraction (XRD) patterns, powder samples were loaded in polyimide (1mm OD Kapton) tubes sealed with clay. The diffraction patterns were obtained at 28-ID-1 PDF (74.53 keV, λ = 0.16635 Å) at National Synchrotron Light Source II (NSLS-II). Dioptas was used to obtain one-dimensional (1D) data from the two-dimensional (2D) scattering patterns.[27] To further determine oxidation state of nickel, oxidized and reduced supported NiO_x catalysts were pressed onto a copper foil and analyzed by X-ray photoelectron spectroscopy (XPS). The instruments consist of an ultra-high vacuum system equipped with a monochromatic Al K-alpha X-ray source and a SPECS Phoibos NAP 150 electron energy analyzer with a 1D delay line detector. When needed, an electron flood gun was used to minimize sample charging.

Catalytic Activity Test

The gas phase reactions were carried out in a fixed bed quartz reactor (OD 9.6 mm, ID 7 mm) packed with sieved catalyst powders at temperature of $25\sim500$ °C under atmosphere pressure. For experiment, a 40 mg of the catalyst was loaded into the quartz reactor and held

in place by quartz wool. Flow rates were measured by mass flow meters (SLA5800 Series, Brooks Instrument) and temperature was monitored by a K-type thermocouple (Omega). Reaction products were identified and analyzed by TRACE™ 1300 GC (Thermo Scientific) containing a capillary column (Carboxen® 1010 PLOT). For the pretreatment, the prepared 10% NiO_x/CeO_2 and 10% Ni/CeO_2 catalysts were treated at 400 °C in He (30 mL min^{-1}) for 30 mins with ramping rate of 10 °C min^{-1}. For the NO reduction by CO reaction, the gases mixtures were 5% NO (20 mL min^{-1} of 10% NO with He balance) and 5% CO (20 mL min^{-1} of 10% CO with He balance). The total flow rate was 40 mL min^{-1} (Space velocity = 60,000 ml/g/hr) in all experiments and a reaction temperature was increased up to 500 °C with ramping rate of 1 °C min^{-1}.

In-situ Diffuse Reflectance Infrared Fourier Transform Spectroscopy (*in-situ* DRIFTS)

The *in-situ* DRIFTS experiments were carried out with a Thermo Scientific Nicolet iS10 FT-IR (4 cm^{-1} spectral resolution, 32 average scans) and a Harrick Praying Mantis chamber. The catalyst sample was first pretreated at 400 °C in flowing He (30 ml min^{-1}) for 30 min. After pretreatment, the sample was cooled to room temperature under He flowing and a background spectrum was taken. The DRIFT data for the NO reduction by CO reaction were collected using the mixtures of 5% NO (20 mL min^{-1} of 10% NO with He balance) and 5% CO (20 mL min^{-1} of 10% CO with He balance) with increasing rate of 1 °C min^{-1} from 25 °C to 500 °C.

Results

Physical properties of the catalysts

In order to understand physical properties of the catalysts, the BET analysis was performed and the specific surface area (SSA), surface density (SD), total pore volume, and

7

average pore diameter are listed in Table 1. The actual Ni loading of oxidized and reduced NiO_x/CeO_2 catalysts were also confirmed by ICP-AES tests and results are included in Table 1. The as-received CeO_2 and CeO_2-Oxi samples show similar SSA, pore volume, and pore size values. Compared to as-received CeO_2, the CeO_2-500R and CeO_2-700R samples show decreased SSA and increased pore diameter due to the sintering of CeO_2, while pore volume was not changed much. Especially, the specific surface area (28 m^2 g^{-1}) and average pore size (10.2 nm) of the CeO_2-700R sample were reduced ~87% and increased ~6 times, respectively, compared to the as-received CeO_2 (216 m^2 g^{-1} and 1.5 nm). It has been reported that bulk CeO_2 shows two reduction peaks at 400~500 ^{o}C and 750~800 ^{o}C, which are corresponding to the reduction of surface and bulk (lattice) oxygen species.[28-31] Based on the reported reduction temperatures of CeO_2, it can be expected that the decreasing of SSA with CeO_2-500R and CeO_2-700R samples is related to the reduction of oxygen species and the particle morphology change (e.g., CeO_2 crystallite size). In the XRD section, a detailed CeO_2 morphology change will be provided. In the case of NiO_x/CeO_2 (oxidized and reduced) samples, the SSAs were lower than that of bulk CeO_2, indicating that pores in CeO_2 were blocked by NiO_x.

ICP-AES elemental analysis of the oxidized and reduced NiO_x/CeO_2 samples showed that Ni loadings were similar to the calculated ones, while 10% NiO_x/CeO_2-700R contained a little higher value than 10 wt%. The calculated Ni surface density (SD, # of Ni atoms/nm^2) using the specific surface area and Ni loading shows that reduced sample's SD values were higher than that of oxidized one. In the case of 10% NiO_x/CeO_2-700R sample, the SD value was ~ 9 times high compared to the oxidized sample due to the low specific surface area.

Table 1 Ni wt% by ICP-AES, specific surface area (SSA), surface density (SD), total pore volume, and average pore size of the bulk CeO_2 and NiO_x/CeO_2 catalysts

Sample	Ni wt %*	SSA (m²/g)	SD (Ni/nm²)**	Total pore volume (cm³/g)	Average Pore Size (nm)
CeO₂ (as-received)	-	216	-	0.16	1.5
CeO₂-Oxi	-	212	-	0.17	1.6
CeO₂-500R	-	180	-	0.17	1.9
CeO₂-700R	-	28	-	0.14	10.2
10% NiOₓ/CeO₂	10.3	180	5.9	0.15	1.7
10% NiOₓ/CeO₂–500R	10.3	142	7.4	0.14	2.0
10% NiOₓ/CeO₂–700R	11.8	23	52.6	0.12	10.3
Bulk NiO	-	32	-	0.06	3.7

* Collected by the ICP-AES measurement

** surface density of Ni $\left({}^{Ni}\!/_{nm^2} \right) = \dfrac{\frac{W_{Ni}}{100} \times 6.02 \times 10^{23} \times \frac{1}{M_{Ni}}}{S \times 10^{18}}$ where W_{Ni} is the weight percentage of Ni by ICP-AES, M_{Ni} is the atomic weight of Ni (58.7 g/mol), and S is the SSA of the oxidized or reduced NiOₓ/CeO₂ sample.

Figure 1 shows the nitrogen adsorption/desorption isotherm curves of bulk CeO₂ and supported NiOₓ on CeO₂ catalysts. The isotherm curves of bulk CeO₂ (as-received and oxidized), CeO₂-500R, 10% NiOₓ/CeO₂, and 10% NiOₓ/CeO₂-500R exhibited type IV isotherm with a H1-type hysteresis loop shape in the range from 0.35 to 0.77 of the relative pressure (P/P⁰), indicating that the NiOₓ/CeO₂ and reduced NiOₓ/CeO₂-500R catalysts possessed mesoporous structure. In the case of bulk CeO₂-700R and 10% NiOₓ/CeO₂-700R, the isotherm curves exhibited type V isotherms with a H3 hysteresis loop at high relative pressure (0.8~1.0) due to silt-shaped

pores and relatively large pore size of 10 nm.[32,33] Note that as the size of mesopore increases, it requires high pressure to completely fill larger pores. The bulk NiO showed type IV isotherm with H4 hysteresis loop, indicating that bulk NiO contained narrow slit-like pore structures.
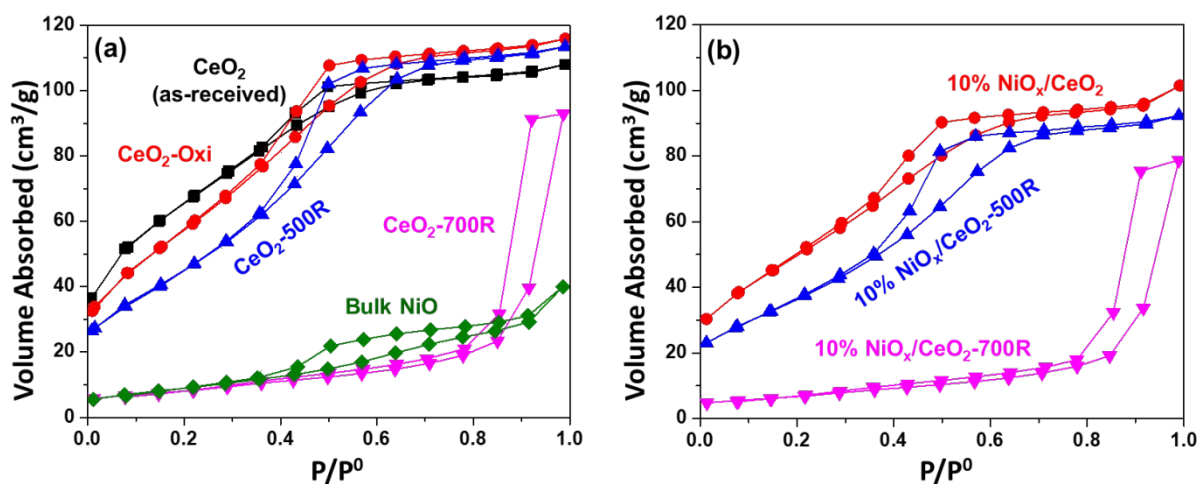

Fig. 1 (a) N_2 adsorption-desorption isotherms of the bulk CeO_2 (as-received), CeO_2-Oxi, CeO_2-500R, CeO_2-700R, and bulk NiO (b) N_2 adsorption-desorption isotherms of the NiO_x/CeO_2 (oxidized and reduced) catalysts.

Raman spectroscopy

Raman spectroscopy has been employed to investigate the molecular structure and bonding vibration of bulk and supported catalysts.[34,35] The Raman spectra of bulk CeO_2, 10% NiO_x/CeO_2 (oxidized and reduced) catalysts, and bulk NiO catalysts are shown in Fig. 2. The dominant peak at ~457 cm^{-1} of bulk CeO_2 corresponded to the intrinsic F_{2g} symmetric vibrational mode of fluorite CeO_2, due to symmetric breathing mode of the oxygen atoms around cerium ions.[36-38] The other weak bands around ~252 cm^{-1}, ~600 cm^{-1}, and ~1034 cm^{-1} were assigned to second-order transverse acoustic (2TA) mode, oxygen vacancy/defect induced (D) mode, and second-order longitudinal optical (2LO) mode, respectively.[39,40] The Raman spectra of bulk NiO exhibited broad band at ~500 cm^{-1} corresponded to one-phonon

longitudinal optical (LO) mode.[41] The Raman band at ~550 cm^{-1} on the 10% NiO$_x$/CeO$_2$ and 10% NiO$_x$/CeO$_2$-500R spectra could be assigned to NiO or oxygen vacancy on CeO$_2$. It was reported that the D mode band in CeO$_2$ spectrum shifted from ~600 cm^{-1} to lower Raman shift at and over 500 °C reduction temperature.[42] Z. Wu et al., used the UV-Raman (325 nm) spectroscopy to understand the developing of defect sites in ceria nanorods and concluded that ~560 cm^{-1} band should be assigned to oxygen vacancy on CeO$_2$ under the reducing conditions.[42] The authors confirmed the presence and recovery of oxygen vacancy upon Raman study of oxygen adsorption. Using the UV-Raman (362.8 nm) spectroscopy, T. Taniguchi et al., observed that the position of D mode band in the bulk CeO$_2$ Raman spectra was not shifted at higher calcination temperature.[43] The authors also reported separated D bands at 550 cm^{-1} (D$_1$ band) and 600 cm^{-1} (D$_2$ band) over Gd^{3+}-doped ceria nanoparticles and independence of I$_D$/I$_{F2g}$ ratio with varying the annealing temperature. Note that both Z. Wu et al., and T. Taniguchi et al., showed the decreasing I$_D$/I$_{F2g}$ ratio with increasing a calcination temperature over bulk CeO$_2$. Although UV-Raman spectroscopy is more sensitive compared to visible Raman to detect the ceria defect site, 532nm visible Raman results show that the D mode band at ~600 cm^{-1} was not shifted with increasing a reduction temperature (Fig. S1 (Supporting Information)). Based on Fig. S1 result, we could reasonably assign the ~550 cm^{-1} to NiO$_x$ related band. In the case of 10% NiO$_x$/CeO$_2$-700R sample, CeO$_2$ F$_{2g}$ peak was dominant, while the NiO$_x$ peak and oxygen vacancy/defect induced (D) mode were disappeared. These results provide that the relative portion of defect sites decreased with increasing reduction temperature and NiO species was reduced to metallic Ni, which is not Raman active. As shown in Fig. 2 (inset), the defect ratio (I$_D$/I$_{F2g}$) follows the sequence 10% NiO$_x$/CeO$_2$ > 10% NiO$_x$/CeO$_2$-500R > 10% NiO$_x$/CeO$_2$-700R, confirmed that oxygen vacancy/defect sites decreased with increasing reduction temperature. Furthermore, the defect ratio of 10% NiO$_x$/CeO$_2$ is higher

than that of bulk CeO_2, suggesting that the defect sites were generated after introducing Ni species on the bulk CeO_2 support.
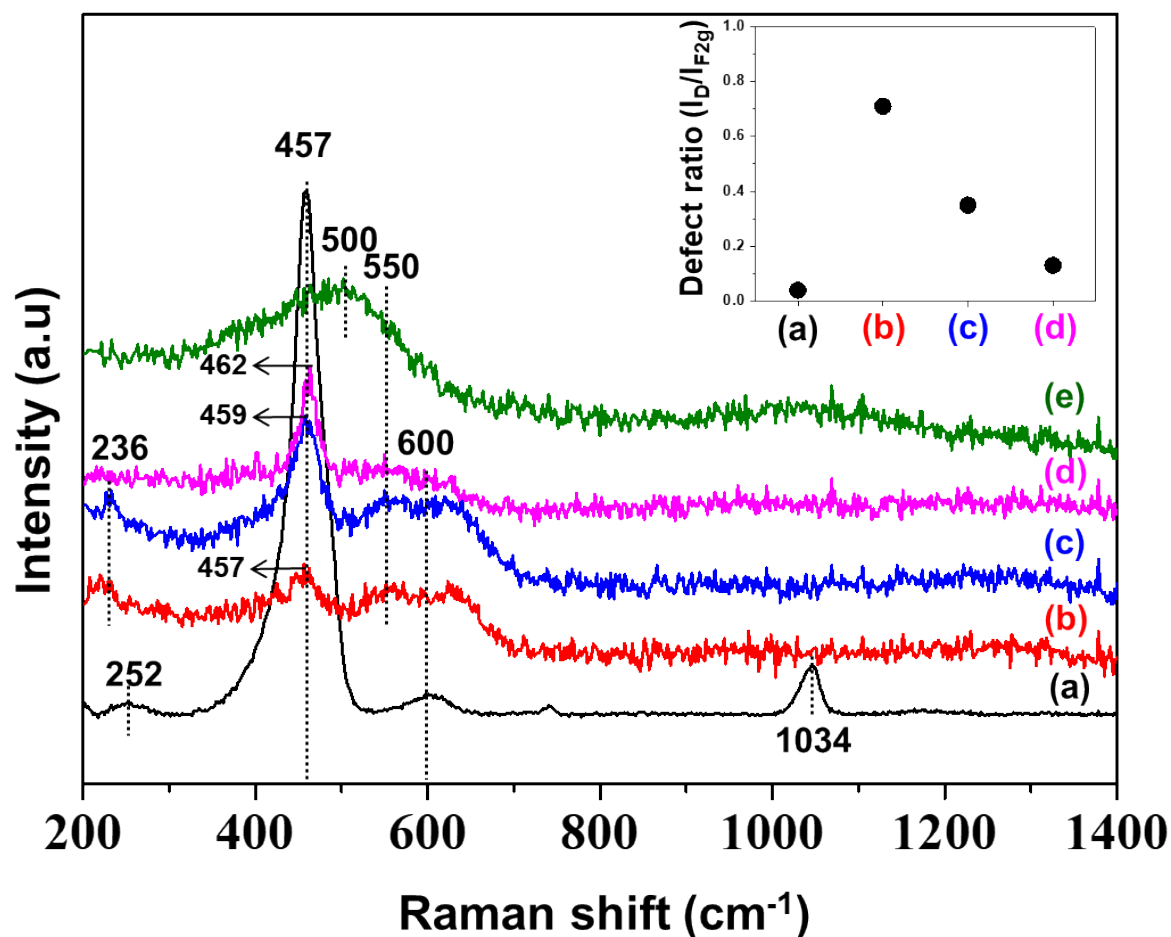

Fig. 2 Raman spectra of (a) Bulk CeO_2 (as-received), (b) 10% NiO_x/CeO_2, (c) 10% NiO_x/CeO_2-500R, (d) 10% NiO_x/CeO_2-700R, and (e) bulk NiO, Inset: defect ratio of (a), (b), (c), and (d) samples. Defect ratio = I_D (~600cm^{-1})/I_{F2g} (~457cm^{-1}).

Powder X-ray diffraction (XRD)

The XRD pattens of the 10% NiO_x/CeO_2, 10% NiO_x/CeO_2-500R, and 10%

NiO_x/CeO_2-700R catalysts are displayed in Fig. 3. For reference, the XRD patterns of the bulk CeO_2, bulk Ni, and bulk NiO samples were also included. The XRD patterns of all the tested catalysts exhibited fluorite CeO_2 patterns (JCPDS-ICDD Card No. 34-394) at 3.0^o, 3.5^o, 4.9^o, 5.8^o, 6.1^o, 7.0^o, 7.6^o, 7.8^o, 8.6^o, and 9.1^o, which are assigned to the (111), (200), (220), (311), (222), (400), (331), (420), (422), and (511) reflections in fluorite structures of CeO_2, respectively. After loading nickel oxide species, the 10% NiO_x/CeO_2 catalysts maintained the fluorite structures of CeO_2, while CeO_2 (111) peak was slightly shifted from $2\theta = 3.045^o$ to $2\theta = 3.056^o$ (bottom left panel in Fig. 3(a)). In addition to the CeO_2 related XRD peaks, new peaks were observed at 3.9^o, 4.5^o, and 6.4^o, which are assigned to the (111), (200), and (220) crystal planes of NiO phase, respectively (JCPDS-ICDD Card No.04-0835). In the case of XRD patterns of reduced NiO_x/CeO_2 catalysts, the metallic Ni peaks (JCPDS-ICDD C and No. 04–0850 (fcc)) were observed at 4.7^o, 5.4^o, 8.9^o, and 9.3^o, which are attributed to (111), (200), (311), and (222) reflections of fcc Ni, respectively. The presence of NiO diffraction peaks in 10% NiO_x/CeO_2-500R spectrum indicates that the sample was not fully reduced to Ni, while the 10% NiO_x/CeO_2-700R sample contained Ni dominantly (bottom right panel in Fig. 3(a)). In addition to the changing of Ni oxidation state, 10% NiO_x/CeO_2-700R sample showed sharp and high intense (or low Full width half maximum (FWHM)) CeO_2 peaks compared to other samples, indicating that the crystallite size of CeO_2 was changed at 700 °C. As shown in Fig. 3(b), the average CeO_2 crystallite size in 10% NiO_x/CeO_2-700R (19.4 nm) was much higher than that of 10% NiO_x/CeO_2 (5.7 nm) and 10% NiO_x/CeO_2-500R (7.2 nm) samples. The oxidized and 500 °C reduced sample's CeO_2 crystallite size were relatively similar to or slightly higher than that of bulk CeO_2 (5.1 nm). The lattice parameter of CeO_2 (5.423 Å) was slightly decreased to 5.403 Å by the Ni loading, while both oxide and reduced samples' lattice parameters were consistent.
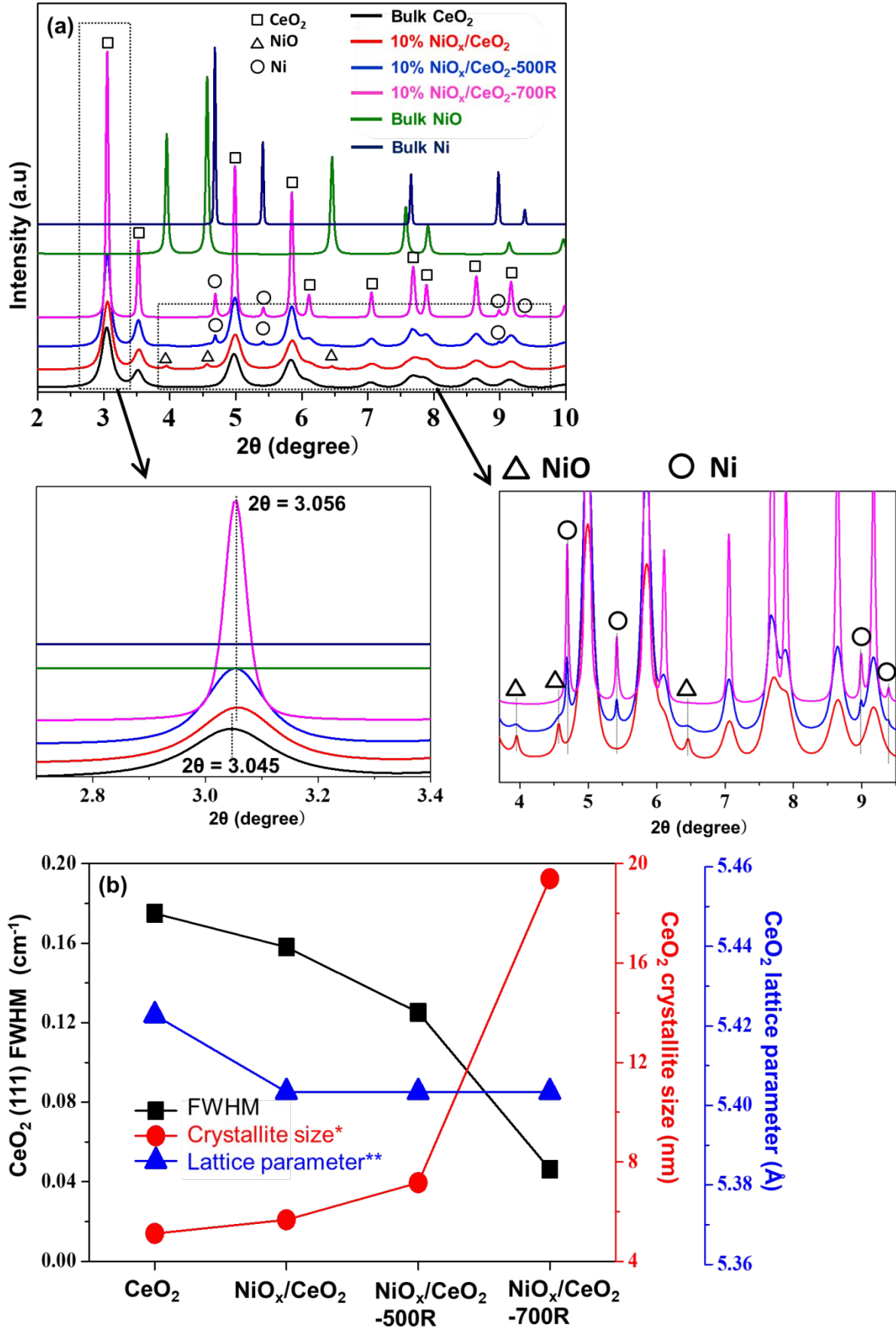
Fig. 3 (a) XRD patterns of bulk CeO_2, 10% NiO_x/CeO_2, 10% NiO_x/CeO_2-500R, 10% NiO_x/CeO_2-700R, bulk NiO, and bulk metallic Ni. NiO and Ni phase are labeled with Δ and O symbol, respectively. (b) CeO_2 (111) Full width half maximum (FWHM, black square), CeO_2 crystallite size (red circle), and CeO_2 lattice parameter (blue triangle).

*: $D = 0.9\lambda/(\beta \cdot cos\theta)$ **: $a = \sqrt{h^2 + k^2 + l^2} \cdot d_{111} = \sqrt{3}d_{111}$, $d_{111} = \frac{\lambda}{2 \cdot sin\theta_{111}}$

D is the crystallite size, λ is the X-ray wavelength (0.16635 Å), β is the FWHM of the CeO_2 (111) peak, θ is the Bragg angle of the peak, a is the lattice parameter, and d is the spacing of (111) lattice planes.

High-resolution transmission electron microscopy (HR-TEM)

Fig. 4 displays the images of high-resolution transmission electron microscopy (HR-TEM) for the NiO_x/CeO_2, NiO_x/CeO_2-500R, and NiO_x/CeO_2-700R samples. The HR-TEM image of 10% NiO_x/CeO_2, in Fig. 4(a), shows lattice fringe with d-spacing of ~2.4 Å corresponding to the (111) plane of NiO particles which were located on the CeO_2 surface. In the case of 10% NiO_x/CeO_2-500R sample, both Ni (d-spacing = ~2.0 Å) and NiO (d-spacing = ~2.4 Å) particles with (111) planes were observed. (Fig. 4(b)) The HR-TEM image of 10% NiO_x/CeO_2-700R catalyst, in Fig. 4(c), shows that CeO_2 particles become bigger due to the agglomeration of CeO_2 at high reduction temperature. Furthermore, fully reduced Ni particles were mainly observed on the CeO_2 surface although we can't ignore the possibility of NiO presence.
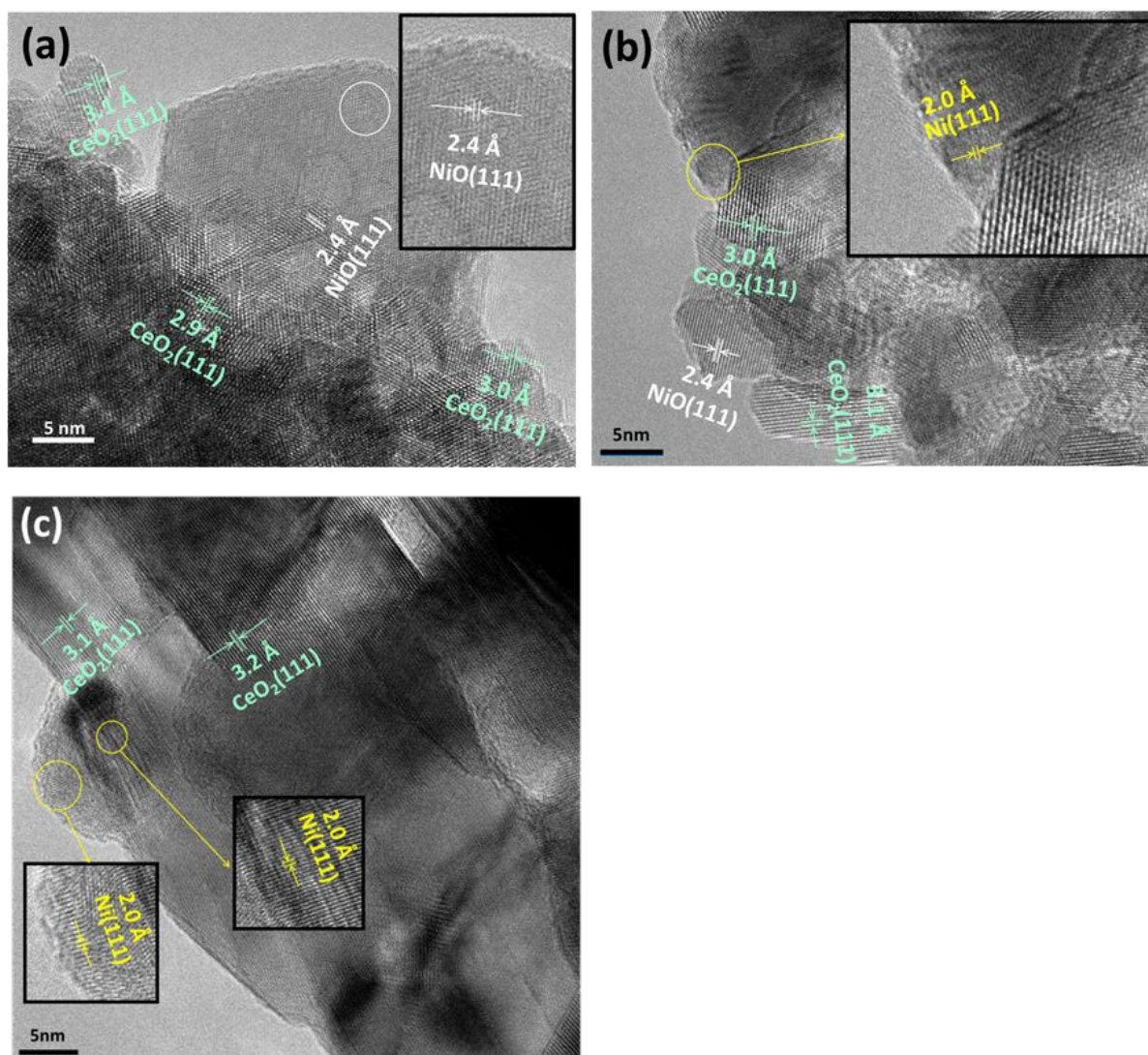
Fig. 4 HR-TEM images for (a) 10% NiO$_x$/CeO$_2$, (b) 10% NiO$_x$/CeO$_2$-500R, and (c) 10% NiO$_x$/CeO$_2$-700R.

To further investigate the morphology and the elemental distributions in oxidized and reduced NiO$_x$/CeO$_2$ catalysts, the high-angle annular dark-field scanning TEM (HAADF-STEM) with corresponding energy-dispersive X-ray spectroscopy (EDS) elemental maps were also collected (Fig. 5 and Fig. S2-S4). The EDS elemental maps of 10% NiO$_x$/CeO$_2$ sample (Fig. 5(a) and S2) show that Ni signal (white circle) is superimposed on O signal, which confirms the existence of NiO on CeO$_2$ surface. In 10% NiO$_x$/CeO$_2$-500R sample (Fig. 5(b) and S3), a

local phase transformation from NiO to Ni is clarified by the disappearance of O in the Ni positions (blue circle). In the case of 10% NiO_x/CeO_2-700R sample, fully reduced Ni phase is displayed at the edge of CeO_2 surface (Fig. 5(c) and S3). It is worthwhile to note that surface NiO_x or Ni particles were agglomerated on the edge of the CeO_2 support in addition to the dispersion on the CeO_2 surface. The changes of Ni particle size at different treatment conditions were further studied with several HAADF-STEM images using image processing software (ImageJ). As shown in particle size distribution histogram (Fig. S5), the average Ni particle size increased with increasing reduction temperature, indicating that the reduction treatment resulted in agglomeration of Ni particle: 17.2 nm (10% NiO_x/CeO_2) < 19.7 nm (10% NiO_x/CeO_2-500R) << 234.5 nm (10% NiO_x/CeO_2-700R). More specifically, the oxidized sample contained a broad ranges of particle size from 0~30 nm, while 20 ~ 25 nm particles were dominant (~40%). The particle size histogram of 500R sample showed the 10~35 nm particle size distribution, while 10 ~ 15 nm and 20 ~ 25 nm particle size showed the higher percentage (~30%) than other values. In the case of 700R catalyst, most nanoparticles (~70%) showed relatively larger size (> 40 nm) and showed two distributions in the range of 40 ~ 45 nm and 150 ~ 200 nm. These results indicated that catalytic activity of CeO_2 supported NiO (or Ni) catalysts could be also affected by the particle size of Ni. On the basis of the characterization results, it is clear that pretreatment condition affects both oxidation state of Ni (i.e., Ni^{2+} and Ni^0) and structural properties of CeO_2 (i.e., particle size) in addition to the physicochemical properties (i.e., SSA).
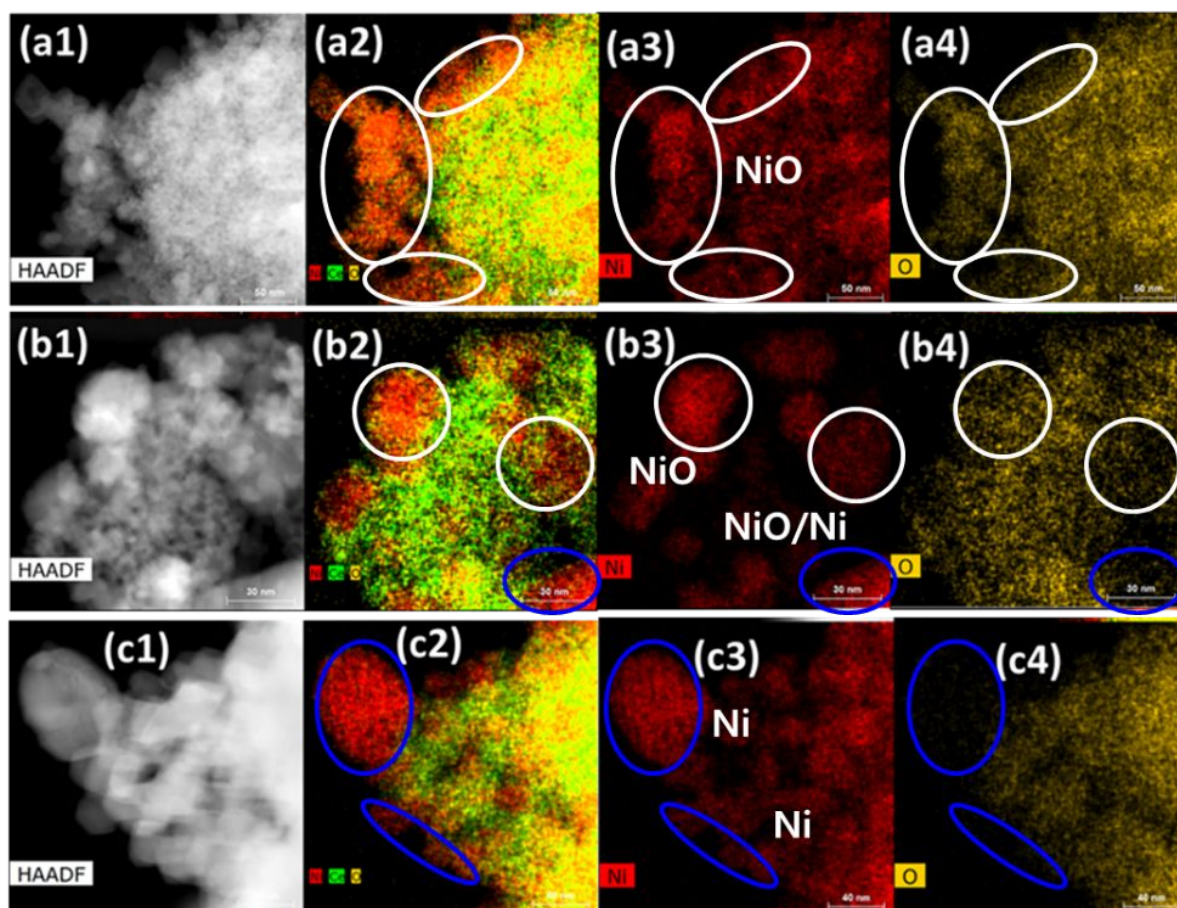
Fig. 5 HAADF-STEM and energy-dispersive X-ray spectroscopy (EDS) elemental mapping of local area of (a) 10% NiO_x/CeO_2, (b) 10% NiO_x/CeO_2-500R, and (c) 10% NiO_x/CeO_2-700R.

The electron energy loss spectroscopy (EELS) has been applied to monitor the oxidation state of Ni qualitatively.[44-47] Fig. 6 shows the Ni L_2 and L_3 edges of oxidized and reduced NiO_x/CeO_2 catalysts, which can be used to evaluate the trends of Ni oxidation states. As shown in Fig. 6(a), the L_2 and L_3 edges of oxidized sample showed sharp and clear peaks, while 500R and 700R samples contained relatively broad L_2 and L_3 edge, due to the agglomeration of Ni particles at high reduction temperature and core excitation in the metal oxide.[44] It has been reported that the intensity ratio (I_{L3}/I_{L2}) between L_3 and L_2 increases with increasing oxidation state of Ni.[45-47] As shown in Fig. 6(b), the I_{L3}/I_{L2} values follow the sequence 4.4 (10%

$NiO_x/CeO_2) > 3.8$ (10% NiO_x/CeO_2-500R) > 3.0 (10% NiO_x/CeO_2-700R) confirming the 700R

sample contains a lower oxidation state of Ni particles than that of oxide and 500R samples.

To further understand oxidation state of nickel, X-ray photoelectron spectroscopy (XPS)

spectra of Ni 2p region of oxidized and reduced supported NiO_x catalysts were obtained (Fig.

S6). On the basis of the spectroscopic and microscopic characterization results, it is clear that

pretreatment condition affects both oxidation state of Ni (i.e., Ni^{2+} and Ni^0) and structural

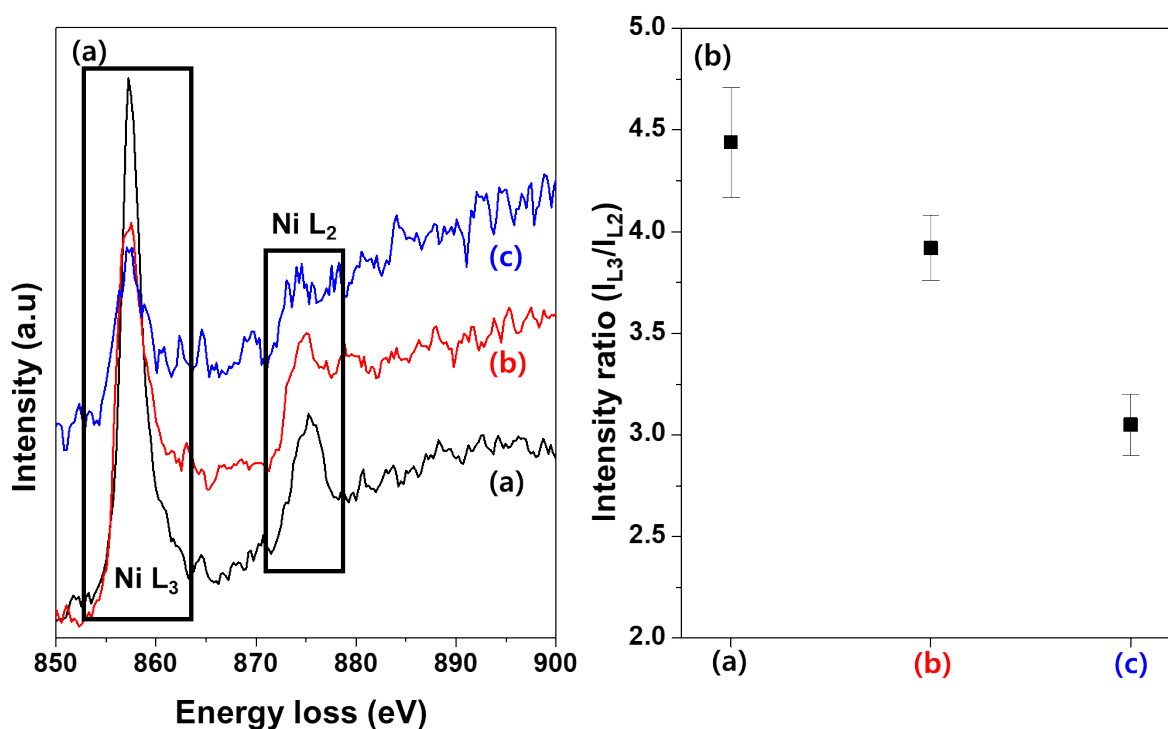properties of CeO_2 (i.e., particle size) in addition to the physicochemical properties (i.e., SSA).

Fig. 6 (a) Corresponding Ni $L_{2,3}$ edges EELS spectra and intensity ratio between L_3 and L_2 with error bars of (a) 10% NiO_x/CeO_2, (b) 10% NiO_x/CeO_2-500R, and (c) 10% NiO_x/CeO_2-700R.

Catalytic Activity tests of NO reduction by CO

NO reduction by CO reaction over the oxidized and reduced NiO_x/CeO_2 catalysts was

performed as the model reaction to understand the molecular and electronic structure relationship with catalytic activity. Fig. 7 shows the conversion and selectivity during the NO reduction by CO reaction as a function of temperature. Both NO and CO conversion increased up to ~100% with an increase in reaction temperature, while NO conversion reached at ~100% at lower temperature compared to the CO conversion one. The NiO_x/CeO_2 catalyst exhibits the best catalytic performance with the NO conversion of 100% at 190 °C, while the NiO_x/CeO_2-500R and NiO_x/CeO_2-700R show the 100% NO conversion at 240 °C and 440 °C, respectively. Pretreatment condition relationship with catalytic activity can be also clarified with T_{50} (reaction temperature at 50% conversion, dot lines in the Fig. 7(a) and (b)). The T_{50} values of both NO conversion and CO conversion were increased continuously with increasing reduction temperature. For example, comparing NiO_x/CeO_2−500R and NiO_x/CeO_2−700R catalysts, the T_{50} values of NO conversion were 185 °C and 260 °C and the T_{50} values of CO conversion were 210 °C and 330 °C, respectively. It was also noticed that the NO conversion was higher than the CO conversion, as shown in Fig. 7(a) and (b), at > 150 °C reaction temperature ranges. The difference of NO and CO conversion results under the reaction temperatures can be explained by the reaction mechanisms. It has been proposed that the NO reduction by CO reaction mechanism is considered to be a two-step reaction (Eq. 1 and 2).[48,49]

$$2NO + CO \rightarrow N_2O + CO_2 \tag{1}$$

$$N_2O + CO \rightarrow N_2 + CO_2 \tag{2}$$

In addition to the NO and CO conversions, the N_2 selectivity and N_2O selectivity were evaluated, and results are shown in Fig. 7(c) and (d). The N_2O was the dominant product at lower NO conversion, while the N_2 selectivity increased with increasing NO conversion at higher reaction temperature. This result indicates that the reaction mechanism or surface

species during the NO reduction by CO reaction on the catalysts could be altered at different reaction temperatures.[50] The N_2 selectivity was also dependent on the pretreatment conditions of samples. Similar to the NO conversion result, the N_2 selectivity was in the order: Oxide > 500R > 700R. It could be deduced that both the SSA and oxygen vacancy sites of the catalysts are crucial factors, which affect the NO adsorption and dissociation, to control a catalytic performance.
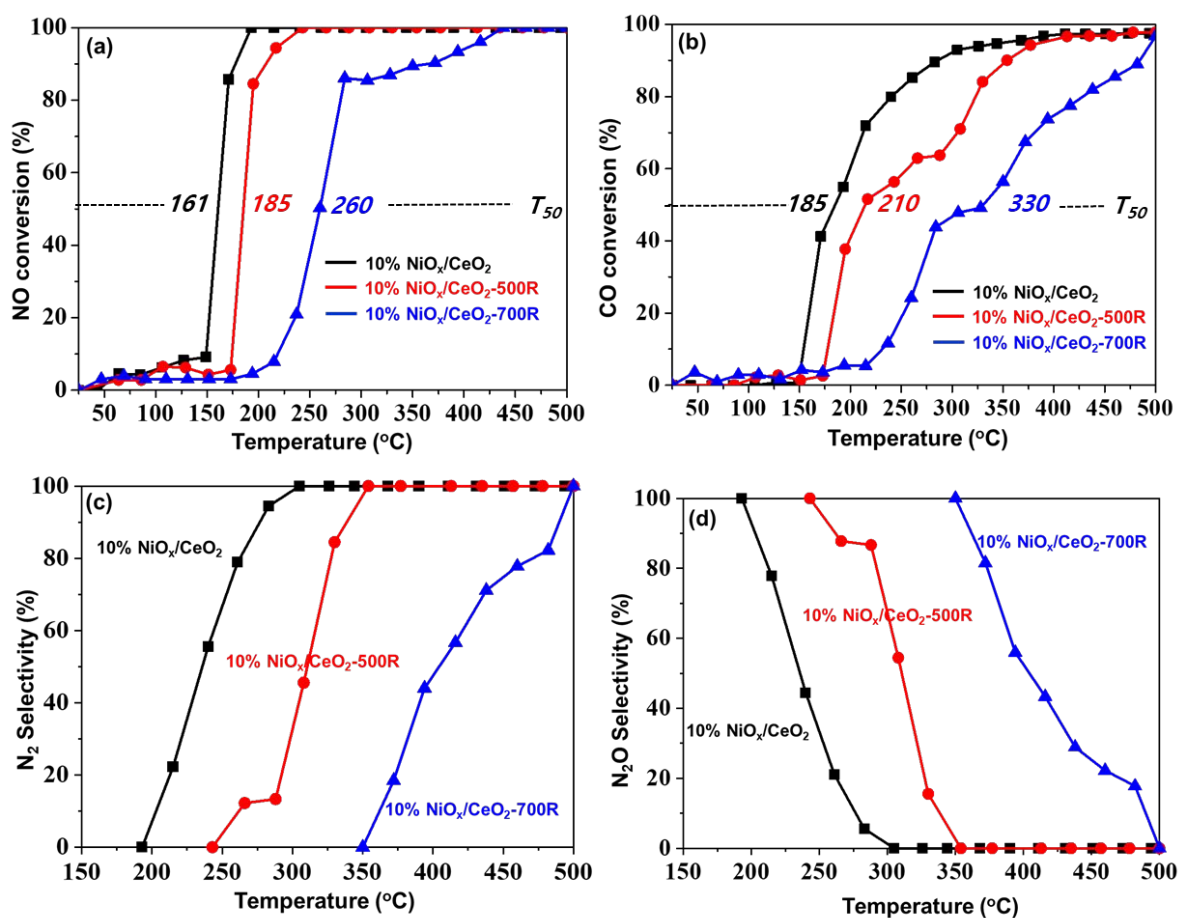

Fig. 7 Catalytic activity of the 10% NiO_x/CeO_2, 10% NiO_x/CeO_2-500R, and 10% NiO_x/CeO_2-700R catalysts in NO reduction by CO reaction at different reaction temperatures. (a) NO conversion, (b) CO conversion, (c) N_2 selectivity, and (d) N_2O selectivity. **Reaction conditions**: 5% NO and 5% CO balanced with helium, Total flow rate = 40 mL/min, Space velocity = 60,000 ml/g/hr.

In-situ Diffuse Reflectance Infrared Fourier Transform Spectroscopy (DRIFTS)

In order to investigate the surface reaction on catalysts and insight of the intermediate species, the *in-situ* DRIFTS of the NO reduction by CO reaction over the oxide and reduced catalysts were recorded from 50 °C to 500 °C. The evolution of spectra and the change of the NO-based surface species, CO-based surface species, and gas phase reactants and products are presented in Fig. 8. Table 2 complies the band position, assignment, and molecular structure of species on the spectra. *In-situ* DRIFTS of oxide and reduced catalysts possess several surface nitrate (NO_3^-) species: bridging bidentate nitrate/O-N-O symmetric vibration (1010 cm^{-1}) and monodentate/bidentate nitrate (1227~1308 cm^{-1} and 1535~1608 cm^{-1}).[14,51,52] Please note that the ~1241 cm^{-1} peak could be also assigned to the linear nitrite (M-O-N=O) peak.[53] In addition to the nitrate peaks, surface nitric oxide peak (O=N-M) at 1677 cm^{-1} is observed at 50 °C over the oxidized and reduced samples' spectra. The intensity of this peak is decreased with increasing temperature and is disappeared at <200 °C (Fig. 8(a), (c), and (e)). Although reduced samples' spectra also possess the surface nitric oxide, the peak intensity is much lower than that of oxide sample. In general, most CO-based peaks (i.e., carbonate and carboxylate) that appear at ≥200 °C are very broad and weak. The bidentate carbonate peak at ~1270 cm^{-1} provids[54] that 10% NiO_x/CeO_2 and 10% NiO_x/CeO_2-500R samples form the CO-based surface species at lower temperature compared to the 10% NiO_x/CeO_2-700R sample. Based on the Fig. 8(a), (c), and (e) spectra, it is expected that NO-based surface species (mostly nitrate) could be adsorbed on the catalyst surface at relatively lower temperature than CO-based surface species (mostly carbonate). The formation of intermediate surface species at different temperature on oxide and reduced catalysts was directly related to the gas phase products as shown in Fig. 8(b, d, and f). The weak and broad bands at 1806~1966 cm^{-1} were assigned to gas phase NO and

disappeared at >200 °C (10% NiO_x/CeO_2), >220 °C (10% NiO_x/CeO_2-500R), and >250 °C (10% NiO_x/CeO_2-700R). In the case of gas phase CO, the broad bands at 2100~2200 cm^{-1} were observed at 50 °C and disappeared at >300 °C(10% NiO_x/CeO_2), >350 °C (10% NiO_x/CeO_2-500R), and >400 °C (10% NiO_x/CeO_2-700R). The intense bands at 2175~2260 cm^{-1} starts showing at 200 °C (10% NiO_x/CeO_2, 10% Ni/CeO_2-500R) and 220 °C (10% Ni/CeO_2-700R), which could be assigned to gas phase N_2O species or NCO intermediate surface species.[55,56] Cheng et al. reported that the NCO could be formed during the NO reduction by CO over NiO/CeO_2, and observed the NCO peak at ~2210 cm^{-1}, which was overlapped with the N_2O bands.[55] The author also reported that NCO species started to form at 170 °C and disappeared at 210 °C. As shown in Fig. 8(b, d, and f), however, the peak intensity at 2175~2260 cm^{-1} started to decrease at >300 °C (10% NiO_x/CeO_2 and 10% NiO_x/CeO_2-500R), while those of 10% NiO_x/CeO_2-700R were retained as the reaction temperature increased up to 500 °C. Therefore, we can reasonably assign the 2175~2260 cm^{-1} to N_2O related band. The peaks at 2295~2489 cm^{-1} can be attributed to the gas phase CO_2 and their intensities were increased with increasing of the reaction temperature.[14,53,57,58] In addition to the gas phase molecules' bands, NO and CO adsorption on surface metal oxide led to the broad peaks at 1823~1837 cm^{-1} (Ni^+/Ni^{2+}-NO), 1990 cm^{-1} (Ni^+-CO), and 2173~2193 cm^{-1} (Ni^{2+}-CO).[55,59] It should be noted that these bands have not been observed with the CeO_2 support.[60] In the case of 10% NiO_x/CeO_2 and 10% NiO_x/CeO_2-500R samples, both Ni^+-CO and Ni^{2+}-CO peak intensity were increased with increasing reaction temperature, while Ni^+/Ni^{2+}-NO peak intensity was decreased. This result indicates that at higher temperature (> 250 °C) the NO, which occupied the active sites (Ni^+ or Ni^{2+}), could be replaced by CO species. For 10% NiO_x/CeO_2-700R sample, weak and broad bands were shown at 1833 cm^{-1} and 2173 cm^{-1}, while the 1990 cm^{-1} was not observed, indicating that CO interaction with active sites was very limited.
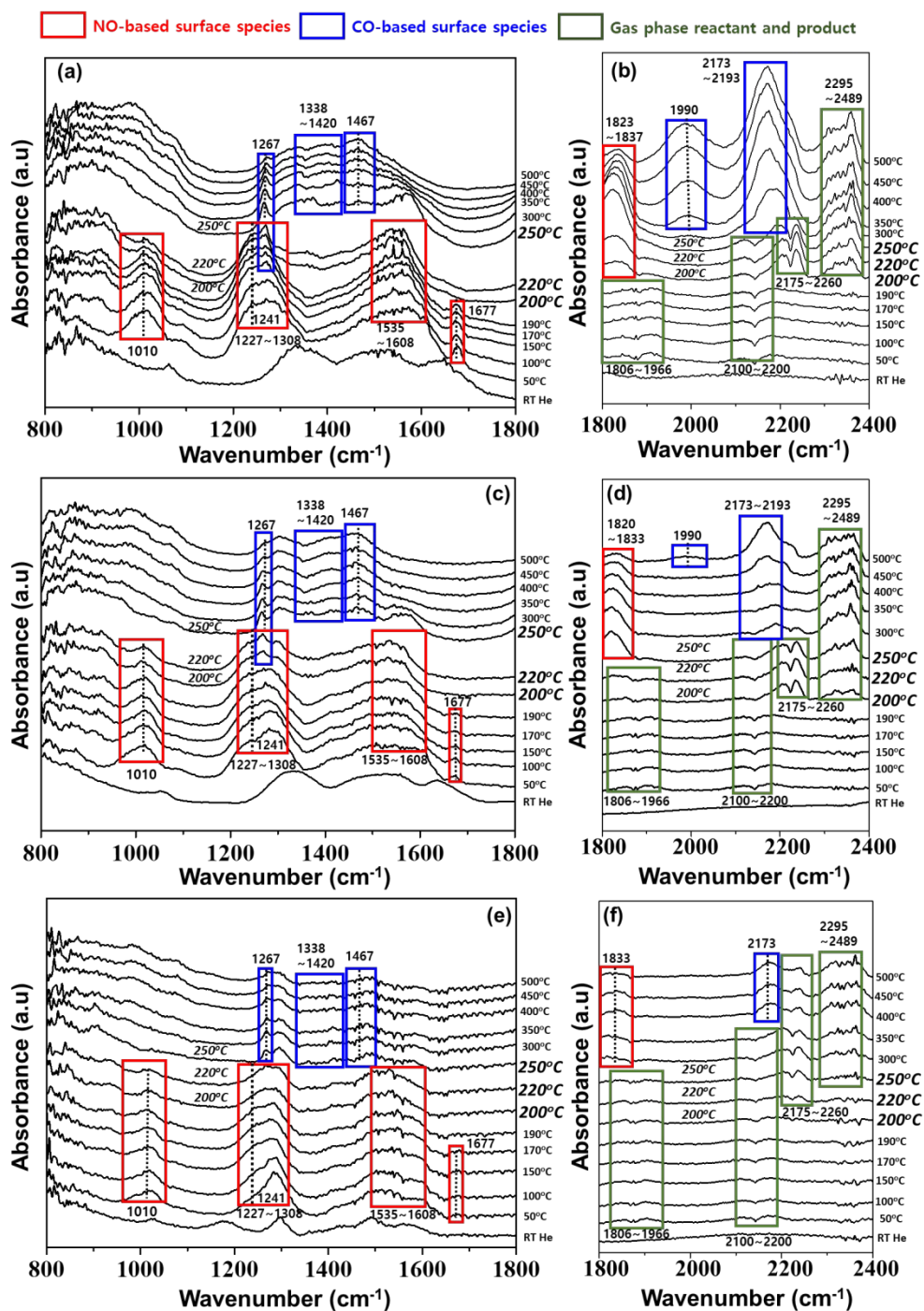
Fig. 8 *in-situ* DRIFTS of (a) 10% NiO_x/CeO_2 (800-1800 cm^{-1}), (b) 10% NiO_x/CeO_2 (1800-2400 cm^{-1}), (c) 10% NiO_x/CeO_2-500R (800-1800 cm^{-1}), (d) 10% NiO_x/CeO_2-500R (1800-2400 cm^{-1}), (e) 10% NiO_x/CeO_2-700R (800-1800 cm^{-1}), and (f) 10% NiO_x/CeO_2-700R (1800-2400 cm^{-1}) in NO reduction by CO at different temperatures. **Reaction conditions**: 5% NO,

5% CO balanced with helium, temperature = 50~500 °C.

Table 2 Peak assignments of the bonding vibrations in the DRIFT spectra

IR wavenumber (cm^{-1})	Assignments	Structure	References
1010	bridging bidentate nitrate, O-N-O symmetric vibration	O=N with O–M and O–M (O-N-O bridging)	14,51,52
1227~1308	bidentate nitrate or linear nitrite or monodentate nitrate	O=N bonded to O, O to M (bidentate) M–O–N=O O,O=N–O–M (monodentate)	14,51-53
1267	bidentate carbonate	O=C bonded to O, O to M	54
1338~1422	monodentate carbonate or carboxylate	O,O=C–O–M (monodentate) $C–O–\overset{\ominus}{O}$	54,61,62
1467	bidentate carbonate	O=C bonded to O, O to M	61,62
1535~1608	monodentate nitrate or bridging nitro or	O,O=N–O–M (monodentate) N bonded to O–M and O–M (bridging nitro)	14,51,52

	bridging bidentate nitrate	$\begin{array}{c} O \\ \| \\ N \\ O \quad O \\ \| \quad \| \\ M \quad M \end{array}$	
1677	Surface nitric oxide	$O{=}N{-}M$	[57]
1823~1837	NO adsorbed on Ni^{2+} (higher cm^{-1}) or Ni^+ (lower cm^{-1})	$Ni^{2+}\text{-}NO$ $Ni^+\text{-}NO$	[55,59]
1806~1966	NO (gas phase molecule)	$N{=}O$	[14,56,63]
1990	CO adsorbed on Ni^+	$Ni^+\text{-}CO$	[59]
2173	CO adsorbed on Ni^{2+}	$Ni^{2+}\text{-}CO$	[59]
2100~2200	CO (gas phase molecule) or CO adsorbed on CeO_x	$C{\equiv}O$ $Ce^{3+}(CO)$	[53,54,57,64]
2175~2260	N_2O (gas phase molecule)	$O{-}N{\equiv}N$	[57]
2295~2489	CO_2 (gas phase molecule)	$O{=}C{=}O$	[14,53,57,58]

Discussion

Structure relationship with catalytic performance

Investigating the physicochemical properties of supported catalyst (i.e., NiO_x/CeO_2) is crucial to understand the relationship between the structures of catalyst and catalytic performance (i.e., NO reduction by CO). The effect of pretreatment on the ceria supported nickel catalysts, which were synthesized by the incipient wetness method, demonstrated that physiochemical properties, molecular structure, and electronic structure were influenced by the reduction temperature. The decreased surface area and increased average pore size of samples, and increased surface density (Table 1) were directly affected by the reduction temperature due

to the blocking of CeO_2 mesopore structure by adding NiO nanoparticles[65] and sintering of CeO_2, especially at 700 °C reduction temperature. In addition to the textural properties, oxygen defect ratio and crystal size (grain growth) of samples were directly affected by the reduction temperature as provided by Raman (Fig. 2 and Fig. S1) and XRD (Fig. 3) results. Hattori et al. investigated the relationship between the heat treatment temperature and the crystal size of CeO_2 using the Raman spectroscopic technique and reported that the peak position of F_{2g} mode of CeO_2 was shifted to higher Raman shift (blue shift) with increasing crystal size, while the linewidth decreased with increasing treatment temperature.[66] Although the peak shift of F_{2g} mode CeO_2 over the oxidized and reduced NiO_x/CeO_2 samples (Fig. 2) were trivial compared to the bulk CeO_2 (Fig. S1) at different reduction temperatures, the Raman results provided that the average crystallite size of CeO_2 was increased with increasing reduction temperatures. Furthermore, XRD results showed clear evidence of the increasing of CeO_2 crystal size (Fig. 3). It has been reported that the F_{2g} mode of CeO_2 shifts to lower energy (red shift) with increasing peak broadness and XRD diffraction peaks shifts to higher 2θ (°) angle with the formation of the M-Ce-O (M = metal, which has a smaller radius than Ce^{4+}) solid solution due to the lattice shrinking of the CeO_2.[22,67-70] For instance, K. Tang et al. synthesized the NiO/CeO_2 catalysts with varied shapes of CeO_2 (i.e., rod- and cube-shaped) and nickel loadings, and claimed the formation of the Ni-Ce-O solid solution with observation of shifting the F_{2g} mode peak to lower energies (or red shift).[22] K. Tang et al. also reported that F_{2g} (~464 cm^{-1}), 2TA (230-260 cm^{-1}), and D (600-640 cm^{-1}) peak positions and intensities were not changed under the oxidizing (O_2 at 300 °C) and reducing (H_2-Ar at 300 °C) conditions although treatment temperature was relatively low. Under the high temperature treatment (500 °C~ 1000 °C) conditions, L. Li et al. reported that the crystallite size of CeO_2 was increased due to the sintering and it was independent on the dopant metals, such as Zr or Gd.[70] L. Li et al. also

concluded that the lattice constant was not changed with increasing calcination temperatures. On the other hands, F. Strnisa et al. reported a reversible (expansion ↔ contraction) nature of CeO_2 structure over NiO/CeO_2-nanorod under reduction and oxidation conditions at the mild temperatures: 300-500 °C reduction and 25 °C oxidation.[71] F. Strnisa et al. claimed that the increasing of lattice parameter under reduction condition could be due to the changing of Ce oxidation state (4+ to 3+) or Ni exsolution. Although the authors showed the decreasing of crystallite size under the reducing conditions, detailed explanations were not provided. Based on the XRD (Fig. 3) and literature results, the presence of solid solutions on the synthesized oxidized and reduced NiO_x/CeO_2 catalysts in the present work could be expected. However, it is worthwhile to note that the evidence of Ni-Ce-O solid-solution using the Raman results could be controversial: peak broadness (consistent to the presence of solid-solution) and blue shift (inconsistent to the presence of solid-solution), although Raman results provided the presence of oxygen vacancy (or defect) that is related to the formation of solid-solution (Fig. 2). In addition to the molecular structure of samples, the changing of oxidation state of Ni species was identified by spectroscopic and microscopic measurements. As provided by the XRD (Fig. 3), HR-TEM (Fig. 4), EDS mapping (Fig. 5 and Fig. S2-S4), EELS (Fig. 6), and XPS (Fig. S6) results, oxidation state of Ni was decreased under the reducing conditions, especially at higher reduction temperature: oxide (Ni^{+2} dominant), 500R (Ni^{+2} and Ni^0 mixed), 700R (Ni^0 dominant). The HR-TEM images of the oxidized and reduced NiO_x/CeO_2 samples also showed well crystallized structure and the particle sizes were increased with increasing reduction temperatures, which was in good agreement with the Raman and XRD results. The obtained physicochemical information as discussed previously could help to understand the catalytic performance (Fig.7). It is obvious that CeO_2 supported NiO (or Ni) catalysts have superior catalytic activity compared to the bulk NiO and bulk CeO_2 (not shown for brevity).

Furthermore, as shown in Fig. 7, the activity of oxide and reduced samples follow: NiO_x/CeO_2 > NiO_x/CeO_2-500R > NiO_x/CeO_2-700R. It has been reported that the formation of an oxygen vacancy is crucial to control an oxidation and reduction catalytic reaction.[72,73] According to previous research[74,75], the dissociation of adsorbed NO species is the vital step for NO reduction by CO, and oxygen vacancy plays an important role in dissociation of NO species by activating N-O bond. Furthermore, the presence of oxygen vacancies on the surface makes possible dissociation of N_2O.[76] With this respect, a high NO and CO conversion over NiO/CeO_2 is in line with its high oxygen vacancy concentration (or high I_D/I_{F2g} ratio) compared to other reduced samples (Fig. 9). Furthermore, the decreased catalytic activity can be possibly influenced by SSAs, surface density, crystallite size, and oxidation state of surface species of samples under the similar loading of surface species and same mass of catalyst.[77-80] As shown in Fig. 9, the high SSAs, low crystallite size, and fully oxidized sample shows the higher catalytic activity (moles of NO converted/time/surface density, 1/s) than other reduced samples. Based on physicochemical properties and activity results, the reduction treatment resulted in blockage pores, CeO_2 agglomeration, and decreased oxygen vacancy/defect sites and oxidation state of Ni, which could reduce the catalytic activity.
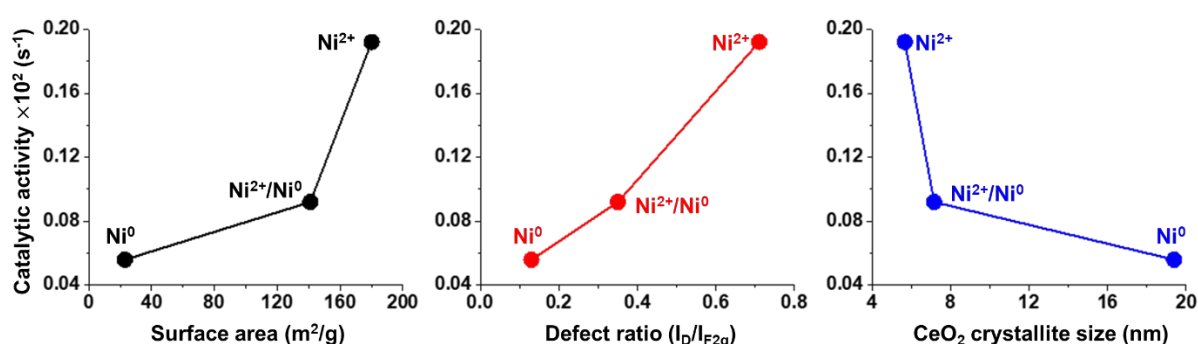

Fig. 9 The catalytic activity* of NO (moles of NO converted/unit time /surface density) at 150 °C (< 10% NO conversion) relationship with specific surface areas, defect ratio, and crystallite size over the 10% NiO_x/CeO_2, 10% NiO_x/CeO_2-500R, and 10% NiO_x/CeO_2-700R catalysts.

$$*: \text{Catalytic activity} = \frac{\text{Conversion} \times \text{NO flow rate} \left(\frac{\text{mol}}{\text{s}}\right)}{\text{Sample amount (g)} \times \text{SSA} \left(\frac{\text{m}^2}{\text{g}}\right) \times \text{SD}\left(\frac{\text{atoms}}{\text{nm}^2}\right) \times 10^{18} \frac{\text{nm}^2}{\text{m}^2} \times \frac{1}{6.022 \times 10^{23}} \frac{\text{mol}}{\text{atoms}}}$$

Intermediate species and Reaction mechanism for the NO reduction by CO

Based on the DRIFT results, the complicated intermediate surface species were formed on both oxide and reduced samples when they were exposed to NO and CO, and peak intensities were varied with the reaction temperature. The intermediate nitrate species bonded to catalyst surface dominantly and kept stable at lower temperature (i.e., ≤200 °C), indicating that adsorbed nitrate species hindered the adsorption of CO to the catalyst surface (Fig. 8(a), (c), and (e)).[56,81,82] Because the different surface NO-based intermediate species (i.e., monodentate/bidentate nitrate and nitrite) were shown simultaneously at the same temperature, it is challengeable to propose the detailed mechanism of intermediates' formation. C. Deng et al., observed multi-NO species during the NO adsorption over CeO_2 and CeCr samples at 25 °C and concluded that chemisorbed NO species could be rearranged.[53] Similar phenomena have been provided from the literatures over ceria supported catalysts, though peak positions were varied with different supported catalysts.[14,53,54,63] For instance, C. Deng et al.[56,83] and X. Cheng et al.[55] reported the presence of multi-nitrate structure at 50 °C and 170 °C over CeO_2-based supported CuO and NiO catalysts, respectively. In addition to the supported catalysts, mixed metal oxide catalysts ($CeMO_x$, M=Co, Fe, Cu, Zr, Mn) also showed the similar results.[52] C. Deng et al. also claimed that oxygen vacancy on catalyst improved the desorption, decomposition and transformation of adsorbed NO species. As shown in Fig. 8(a), (c), and (e), however, the temperatures of appearance and disappearance of the NO species on oxide and reduced samples were very similar, providing that these temperatures were not controlled by the oxygen vacancy under the tested samples and experimental conditions. Please note again

that oxygen vacancy concentration was changed with following order: 10% NiO_x/CeO_2 > 10% NiO_x/CeO_2-500R > 10% NiO_x/CeO_2-700R. Although oxygen vacancy was not much related to the temperature of formation and decomposition of NO-based intermediate species, however, it could be related to the CO-based intermediate (i.e., carbonate at 1267 cm^{-1}) formation temperature as well as the amount of nitrate formation (i.e., peak intensity of nitrate at 1241 cm^{-1}): Carbonate formation temperature (10% NiO_x/CeO_2 < 10% NiO_x/CeO_2-500R < 10% NiO_x/CeO_2-700R) and Nitrate (1241 cm^{-1}) peak intensity (10% NiO_x/CeO_2 > 10% NiO_x/CeO_2-500R > 10% NiO_x/CeO_2-700R). In addition, compared with reduced samples, 10% NiO_x/CeO_2 showed much higher peak intensity of NO-adsorption and CO-adsorption on active sites at 1823~1837 cm^{-1} (Ni^{2+}/Ni^+-NO), 1990 cm^{-1} (Ni^+-CO), and 2173 cm^{-1} (Ni^{2+}-CO) at >200 °C (Fig. 8(b), (d), (f)). X. Cheng et al. reported that the N_2O formation is related to the Ni^+-NO species.[55] As shown in Fig. 8 ((b), (d), and (f)), the N_2O appeared at same (10% NiO_x/CeO_2) or lower (10% NiO_x/CeO_2-500R and 10% NiO_x/CeO_2-700R) temperature compared to the Ni^{2+}/Ni^+-NO peak appearance temperature. The N_2O disappearance temperature, however, was far lower than that of Ni^{2+}/Ni^+-NO peak, indicating that the N_2O formation was not directly related to the Ni^{2+}/Ni^+-NO species. Please note that 10% NiO_x/CeO_2-700R sample's N_2O peak intensity decreased from 300 °C, but it was retained up to 500 °C. In the case of CO_2 formation, it is expected that (1) carbonate surface species converted into CO_2 directly, (2) Ni^{2+}-NO species interacts with carbonate (i.e., 1267 cm^{-1}) species and forms the CO_2 and Ni^{2+}-CO (2173~2193 cm^{-1}) species, or (3) gas-phase CO interacts with nitrate/nitrite to form CO_2. Although we admit that in-situ XPS can provide the oxidation state of Ni in detail, in-situ DRIFT could provide the Ni oxidation state indirectly. Based on the peak position and intensity of 1823~1837 cm^{-1} (Ni^{2+}/Ni^+-NO), 1990 cm^{-1} (Ni^+-CO), and 2173 cm^{-1} (Ni^{2+}-CO), it is expected that both Ni^+ and Ni^{2+} were presence on the 10% NiO_x/CeO_2 sample, while the 500R and 700R samples mainly

contain Ni^{2+} at high reaction temperature (i.e., > 200 °C). The DRIFT results clearly provided that oxidation state of Ni was critical to enhance the catalytic performance, which was also supported by XRD (Fig. 3), TEM (Fig. 4 and 5), EELS (Fig. 6), XPS (Fig. S6) and activity results (Fig. 7).

The specific reaction mechanisms under NO reduction by CO reaction over supported noble and transition metal oxide catalysts have been proposed and it has been widely accepted that NO dissociation is the crucial step.[63,79,80] Y. Wang et al., proposed that dissociated NO (N* and O*) on oxygen vacancy sites, which is generated by CO reaction with surface oxygen, could produce N_2 (N* + N* → N_2 + 2*) and N_2O (NO* + N* → N_2O + 2*) without interaction with CO, while adsorbed NO (i.e., NO* or NO_x*) on Ce^{3+}-oxygen defect site associatively could not produce N_2.[21] Although atomic level reaction mechanisms could not be provided directly, in our case, molecular level reaction mechanisms could be proposed by combining the DRIFT and activity results. It is hypothesized that both oxidized and reduced catalysts follow same reaction mechanism pathways during the NO reduction by CO reaction: *N_2O decomposition and N_2 formation*: (1) NO → nitrate/nitrate on CeO_2 surface (≤50 °C~200 °C), (2) nitrate/nitrite → N_2O (200~250 °C, under reducing condition by CO), (3) N_2O → N_2 + Ni-NO (>200 °C), *CO_2 formation*: (1) CO → carbonate on CeO_2 surface (≥200 °C), (2) carbonate → CO_2 + Ni-CO. However, these reaction mechanisms were favor on the oxide active species compared to the reduced one. Based on DRIFT results, at higher temperature (>200 °C), it could be expected that both Ni^+ and Ni^{2+} were presence on the oxide samples, while the reduced samples (500R and 700R) mainly contain Ni^{2+}, indicating that Ni^+ greatly affected the catalytic activity (at reaction step (3) of N_2O decomposition and N_2 formation, at reaction step (2) of CO_2 formation).

Conclusions

In this work, the impact of pretreatment conditions on structure of NiO_x/CeO_2 catalysts, which was directly related to the NO reduction by CO reaction, was investigated. The physical properties (SSA, pore volume, pore size, and crystallite size), molecular structure, oxidation state of active sites, and catalytic activity were controlled by the pretreatment conditions. From BET (Table 1) and XRD (Fig. 3), it was clearly observed that SSA decreased and crystallite size of CeO_2 support increased with increasing reduction temperature, due to agglomeration and migration of CeO_2 support. The EDS elemental mapping (Fig. 5), EELS (Fig. 6), XPS (Fig. S6), and XRD provided the formation of metallic Ni species and it became larger and clearer as the reduction temperature increased. By combining the physiochemical properties and catalytic activity (Fig. 7) results, it could be concluded that the decreased catalytic activity of reduced NiO_x/CeO_2 catalysts was caused by lower specific surface area, less oxygen vacancy/defect sites (Raman, Fig. 2) and exposure of reduced metallic Ni on the surface. From *in-situ* DRIFTS (Fig. 8) and activity results, the possible reaction mechanisms for NO reduction by CO were proposed. At lower reaction temperature (i.e., < 200 ºC), NO-based surface species, mainly nitrate, was dominant and it converted to N_2O with increasing the temperature (i.e., <200 ºC). CO-based surface species, mainly carbonate, occupied the active (or support) sites after nitrate converted to N_2O. Consequently, N_2O decomposition led N_2 formation. CO_2 production temperature was matched for the carbonate formation, indicating that carbonate transformation and nitrate interaction with CO could cause the CO_2 formation.

Conflicts of interest

There are no conflicts of interest to declare.

Acknowledgements

Author contributions

K.L.; Methodology, Writing-original draft, Formal Analysis, G.K.; Methodology, Writing-original draft, S.H.; Methodology, Writing-original draft, Writing-review&editing, G.B.; Methodology, Writing-original draft, T.K.; Writing-review&editing, Supervision, Formal Analysis. All authors have read and agreed to the published version of the manuscript

Reference

1. M. V. Twigg, *Appl. Catal. B,* 2007, **70**, 2-15.
2. X. Yao, C. Tang, F. Gao and L. Dong, *Catal. Sci. Technol.,* 2014, **4**, 2814-2829.
3. A. L. Karemore, P. D. Vaidya, R. Sinha and P. Chugh, *Int. J. Hydrogen Energy*, 2016, **41**, 22963-22975.
4. M. Chen, L. Fan, L. Qi, X. Luo, R. Zhou and X. Zheng, *Catal. Commun.,* 2009, **10**, 838-841.
5. X. Yao, Y. Xiong, W. Zou, L. Zhang, S. Wu, X. Dong, F. Gao, Y. Deng, C. Tang and Z. Chen, *Appl. Catal. B,* 2014, **144**, 152-165.
6. Y. Fu, Y. Tian and P. Lin, *J. Catal.*, 1991, **132**, 85-91.
7. K. C. Taylor and J. C. Schlatter, *J. Catal.*, 1980, **63**, 53-71.
8. N. Takahashi, H. Shinjoh, T. Iijima, T. Suzuki, K. Yamazaki, K. Yokota, H. Suzuki, N. Miyoshi, S.-i. Matsumoto and T. Tanizawa, *Catal. Today*, 1996, **27**, 63-69.
9. N. W. Cant, D. E. Angove and D. C. Chambers, *Appl. Catal. B,* 1998, **17**, 63-73.
10. A. Srinivasan and C. Depcik, *Cataly. Rev.,* 2010, **52**, 462-493.
11. A. Srinivasan and C. Depcik, *Surf. Rev. Lett.,* 2012, **19**, 1230001.
12. Y. Cao, R. Ran, X. Wu, X. Wu, J. Wan and D. Weng, *Catal. Today*, 2017, **281**, 490-499.
13. T. Chafik, D. I. Kondarides and X. E. Verykios, *J. Catal.*, 2000, **190**, 446-459.
14. L. Liu, B. Liu, L. Dong, J. Zhu, H. Wan, K. Sun, B. Zhao, H. Zhu, L. Dong and Y. Chen, *Appl. Catal. B,* 2009, **90**, 578-586.
15. A. Giannakas, A. Ladavos and P. Pomonis, *Appl. Catal. B,* 2004, **49**, 147-158.
16. J.-Q. Lu, C.-X. Sun, N. Li, A.-P. Jia and M.-F. Luo, *Appl. Surf. Sci.,* 2013, **287**, 124-134.
17. T.-Z. Ren, P.-B. Xu, Q.-F. Deng and Z.-Y. Yuan, *React. Kinet. Mech. Catal.,* 2013, **110**, 405-420.
18. R. Zhang, W. Y. Teoh, R. Amal, B. Chen and S. Kaliaguine, *J. Catal.*, 2010, **272**, 210-219.
19. L. Ma, M.-F. Luo and S.-Y. Chen, *Appl. Catal. A,* 2003, **242**, 151-159.
20. L. Liotta, G. Pantaleo, G. Di Carlo, G. Marcı and G. Deganello, *Appl. Catal. B,* 2004, **52**, 1-10.
21. Y. Wang, A. Zhu, Y. Zhang, C. Au, X. Yang and C. Shi, *Appl. Catal. B,* 2008, **81**, 141-149.
22. K. Tang, W. Liu, J. Li, J. Guo, J. Zhang, S. Wang, S. Niu and Y. Yang, *ACS App. Mater. Interfaces,* 2015, **7**, 26839-26849.
23. C. Tang, B. Sun, J. Sun, X. Hong, Y. Deng, F. Gao and L. Dong, *Catal. Today*, 2017, **281**, 575-582.
24. C. Tang, J. Li, X. Yao, J. Sun, Y. Cao, L. Zhang, F. Gao, Y. Deng and L. Dong, *Appl. Catal. A,* 2015, **494**, 77-86.
25. A. Wolfbeisser, O. Sophiphun, J. Bernardi, J. Wittayakun, K. Fottinger and F. Rupprechter, *Catal. Today*, 2016, **277**, 234-245.
26. D. Lopes, F. Zotin and L. A. Palacio, *Appl. Catal. B,* 2018, **237**, 327-338.
27. C. Prescher and V. B. Prakapenka, *High Press. Res.,* 2015, **35**, 223-230.
28. D. Li, K. Li, R. Xu, X. Zhu, Y. Wei, D. Tian, X. Cheng and H. Wang, *ACS Appl. Mater. Interfaces,* 2019, **11**, 19227-19241.
29. J. Wang, M. Shen, J. Wang, J. Gao, J. Ma and S. Liu, *Catal. Today*, 2011, **175**, 65-

71.

30. S. Zhang, J. Lee, D. H. Kim and T. Kim, *Mol. Catal.,* 2020, **482**, 110703.
31. M. Li and A. C. van Veen, *Appl. Catal. B,* 2018, **237**, 641-648.
32. T. Xu, J. Xue, X. Zhang, G. He and H. Chen, *Appl. Surf. Sci.,* 2017, **402**, 294-300.
33. X. Xu, J. Shen, N. Li and M. Ye, *Int. J. Hydrogen Energy*, 2015, **40**, 13003-13013.
34. B. M. Reddy, A. Khan, Y. Yamada, T. Kobayashi, S. Loridant and J. C. Volta, *J. Phys. Chem. B*, 2002, **106**, 10964-10972.
35. B. M. Reddy, A. Khan, Y. Yamada, T. Kobayashi, S. Loridant and J. C. Volta, *J. Phys. Chem. B*, 2003, **107**, 5162-5167.
36. W. Weber, K. Hass and J. McBride, *Phys. Rev. B*, 1993, **48**, 178-185.
37. J. E. Spanier, R. D. Robinson, F. Zhang, S. W. Chan and I. P. Herman, *Phys. Rev. B*, 2001, **64**, 245407.
38. B. M. Reddy, A. Khan, Y. Yamada, T. Kobayashi, S. Loridant and J. C. Volta, *J. Phys. Chem. B*, 2003, **107**, 5162-5167.
39. M. Daniel and S. Loridant, *J. Raman Spectrosc.,* 2012, **43**, 1312-1319.
40. I. Kosacki, T. Suzuki, H. U. Anderson and P. Colomban, *Solid State Ion.,* 2002, **149**, 99-105.
41. N. Mironova-Ulmane, A. Kuzmin, I. Steins, J. Grabis, I. Sildos and M. Pärs, *J. Physics: Conference Series*, 2007, **93**, 012039.
42. Z. Wu, M. Li, J. Howe, H. M. Meyer III and S. H. Overbury, *Langmuir*, 2010, **26**, 16595-16606.
43. T. Taniguchi, T. Watanabe, N. Sugiyama, A. Subramani, H. Wagata, N. Matsushita and M. Yoshimura, *J. Phys. Chem. C*, 2009, **113**, 19789-19793.
44. R. D. Leapman, L. Grunes and P. Fejes, *Physical Review B*, 1982, **26**, 614.
45. G. Evmenenko, T. T. Fister, F. C. Castro, X. Chen, B. Lee, D. B. Buchholz, V. P. Dravid, P. Fenter and M. J. Bedzyk, *Physical Chemistry Chemical Physics*, 2019, **21**, 8897-8905.
46. S. Hwang, S. M. Kim, S. M. Bak, B. W. Cho, K. Y. Chung, J. Y. Lee, W. Chang and E. A. Stach, *ACS applied materials & interfaces*, 2014, **6**, 15140-15147.
47. E. Dickey, X. Fan and S. Pennycook, *Acta materialia*, 1999, **47**, 4061-4068.
48. C. Deng, J. Qian, C. Yu, Y. Yi, P. Zhang, W. Li, L. Dong, B. Li and M. Fan, *RSC Adv.,* 2016, **6**, 113630-113647.
49. L. Liotta, G. Pantaleo, G. Di Carlo, G. Marci and G. Deganello, *Appl. Catal. B,* 2004, **52**, 1-10.
50. Z. Xu, Y. Li, Y. Lin and T. Zhu, *Environ. Sci. Pollut. Res.,* 2020, **27**, 6723-6748.
51. X. Zhang, H. He, H. Gao and Y. Yu, *Spectrochim. Acta A Mol. Biomol. Spectrosc.,* 2008, **71**, 1446-1451.
52. X. Dai, W. Jiang, W. Wang, X. Weng, Y. Shang, Y. Xue and Z. Wu, *Chinese J. Catal.,* 2018, **39**, 728-735.
53. C. Deng, M. Li, J. Qian, Q. Hu, M. Huang, Q. Lin, Y. Ruan, L. Dong, B. Li and M. Fan, *Chem. Asian J.,* 2016, **11**, 2144-2156.
54. N. Liu, X. Chen, J. Zhang and J. W. Schwank, *Catal. Today*, 2015, **258**, 139-147.
55. X. Cheng, A. Zhu, Y. Zhang, Y. Wang, C. Au and C. Shi, *Appl. Catal. B,* 2009, **90**, 395-404.
56. C. Deng, B. Li, L. Dong, F. Zhang, M. Fan, G. Jin, J. Gao, L. Gao, F. Zhang and X.

Zhou, *Phys. Chem. Chem. Phys.*, 2015, **17**, 16092-16109.

57.   X. Cheng, Y. Cheng, Z. Wang and C. Ma, *Fuel*, 2018, **214**, 230-241.

58.   L. Liu, Z. Yao, Y. Deng, F. Gao, B. Liu and L. Dong, *ChemCatChem*, 2011, **3**, 978-989.

59.   M. Mihaylov, K. Chakarova and K. Hadjiivanov, *J. Catal.*, 2004, **228**, 273-281.

60.   S. Zhang, Y. Li, J. Huang, J. Lee, D. H. Kim, A. I. Frenkel and T. Kim, *J. Phys. Chem. C*, 2019, **123**, 7166-7177.

61.   L. Zhang, X. Yao, Y. Lu, C. Sun, C. Tang, F. Gao and L. Dong, *J. Colloid Interface Sci.,* 2018, **509**, 334-345.

62.   S. Gaur, H. Wu, G. G. Stanley, K. More, C. S. Kumar and J. J. Spivey, *Catal. Today*, 2013, **208**, 72-81.

63.   X. Zhang, X. Cheng, C. Ma and Z. Wang, *Catal. Sci. Technol.,* 2018, **8**, 3336-3345.

64.   C. Kladis, S. K. Bhargava, K. Foger and D. B. Akolekar, *J. Mol. Catal. A Chem.,* 2001, **175**, 241-248.

65.   N. Rui, X. Zhang, F. Zhang, Z. Liu, X. Cao, Z. Xie, R. Zou, S. D. Senanayake, Y. Yang and J. A. Rodriguez, *Appl. Catal. B,* 2021, **282**, 119581.

66.   T. Hattori, K. Kobayashi and M. Ozawa, *Jpn. J. Appl. Phys.,* 2016, **56**, 01AE06.

67.   P. Venkataswamy, D. Jampaiah, D. Mukherjee, C. Aniz and B. M. Reddy, *Catal. Lett.,* 2016, **146**, 2105-2118.

68.   Y. Lee, G. He, A. J. Akey, R. Si, M. Flytzani-Stephanopoulos and I. P. Herman, *J. Am. Chem. Soc.,* 2011, **133**, 12952-12955.

69.   S. Chang, M. Li, Q. Hua, L. Zhang, Y. Ma, B. Ye and W. Huang, *J. Catal.*, 2012, **293**, 195-204.

70.   L. Li, F. Chen, J.-Q. Lu and M.-F. Luo, *J. Phys. Chem. A,* 2011, **115**, 7972-7977.

71.   F. Strniša, V. T. Sagar, P. Djinović, A. Pintar and I. Plazl, *Chem. Eng. J.,* 2021, **413**, 127498.

72.   F. M. Pinto, V. Y. Suzuki, R. C. Silva and F. A. La Porta, *Front. Mater. Sci.,* 2019, **6**, 260.

73.   A. Ruiz Puigdollers, P. Schlexer, S. Tosoni and G. Pacchioni, *ACS Catal.,* 2017, **7**, 6493-6513.

74.   A. G. Makeev and N. V. Peskov, *Appl. Catal. B,* 2013, **132**, 151-161.

75.   Y. Xiong, X. Yao, C. Tang, L. Zhang, Y. Cao, Y. Deng, F. Gao and L. Dong, *Catal. Sci. Technol.,* 2014, **4**, 4416-4425.

76.   W. K. Chen, B. Z. Sun, X. Wang and C. H. Lu, *J. Theor. Comput. Chem.,* 2008, **7**, 263-276.

77.   D. Chan, S. Tischer, J. Heck, C. Diehm and O. Deutschmann, *Appl. Catal. B,* 2014, **156**, 153-165.

78.   C. Gregor, M. Hermanek, D. Jancik, J. Pechousek, J. Filip, J. Hrbac and R. Zboril, *Eur. J. Inorg. Chem*, 2010, **2010**, 2343-2351.

79.   L. Savereide, S. L. Nauert, C. A. Roberts and J. M. Notestein, *J. Catal.*, 2018, **366**, 150-158.

80.   P. Bernard, P. Stelmachowski, P. Broś, W. Makowski and A. Kotarba, *J. Chem. Educ.,* 2021, **98**, 935-940.

81.   Y. Xiaojiang, Y. Xiong, S. Jingfang, G. Fei, D. Yu, T. Changjin and D. Lin, *J. Rare Earchs,* 2014, **32**, 131-138.

82.   X. Yao, F. Gao, Q. Yu, L. Qi, C. Tang, L. Dong and Y. Chen, *Catal. Sci. Technol.,* 2013, **3**, 1355-1366.

83.   C. Deng, Q. Huang, X. Zhu, Q. Hu, W. Su, J. Qian, L. Dong, B. Li, M. Fan and C. Liang, *Appl. Surf. Sci.,* 2016, **389**, 1033-1049.